Characterization of the miniPlanacon XPM85112-S-R2D2 MCP-PMT with custom modified backend electronics

T. Komárek[a], V. Urbášek[b], A. Brandt[c], K. Černý[a], V. A. Chirayath[c], J. DeFazio[d], V. Georgiev[e], S. Hail[c], M. Hrabovský[a], Z. Kubík[e], L. Nožka[a], D. Orlov[f], S. Duarte Pinto[f], M. Rijssenbeek[g], T. Sýkora[h], F. Yang[c], J. Zich[e]

[a]*Joint Laboratory of Optics, Palacky University, 17. listopadu 50A, Olomouc, 77207, Czech Republic*
[b]*Institute of Physics of the Academy of Science of the Czech Republic, Na Slovance 2, Prague 8, 18221, Czech Republic*
[c]*The University of Texas at Arlington, Dept. of Physics, 701 S. Nedderman Drive, Arlington, 76019, TX, USA*
[d]*Photonis Defense Inc., 1000 New Holland Ave, Lancaster, 17601, PA, USA*
[e]*University of West Bohemia, Dept. of Electronics and Informatics, Univerzitní 26, Pilsen, 30100, Czech Republic*
[f]*Photonis Netherlands B.V., Dwazziewegen 2, Roden, 9301 ZR, Netherlands*
[g]*Stony Brook University, Dept. of Physics and Astronomy, Nicolls Road, Stony Brook, 11794, NY, USA*
[h]*Charles University, Faculty of Mathematics and Physics, Ke Karlovu 3, Prague, 12116, Czech Republic*

Abstract

We report the results of the measurements of three pieces of the new Photonis miniPLANACON microchannel-plate photomultipliers (MCP-PMTs) intended for use in the demanding environment of the Large Hadron Collider (LHC) beamline as a part of the AFP Time-of-Flight detector. These photomultipliers were modified in cooperation with the manufacturer by using a custom backend and were subjected to numerous tests, with the focus on the rate capability and crosstalk behaviour. We determined that the two of them with a lower MCP resistance are able to operate without significant saturation at an anode current density of $1\,\mu\text{A/cm}^2$. These two are, therefore, suitable for the intended use and are currently installed as part of the AFP detector packages.

Preprint submitted to NIM A (to be done) *July 7, 2022*

1. Introduction

Photomultiplier tubes (PMTs) are widely used in particle and astroparticle physics experiments for the detection of low photon fluxes. Among them, microchannel-plate photomultipliers (MCP-PMTs) are preferred in many fields of application because they have these main advantages: (1) A fast response in tens of picoseconds (in terms of transit-time spread) thanks to the short distances the electrons have to travel and its high electric field (tens of kV/cm); (2) Insensitivity to magnetic fields even above 1 T [1] thanks to the same reasons; and (3) High spatial resolution thanks to the granularity of the microchannel plates allowing for pixelization through the use of multiple anode pads.

MCP-PMTs, however, also have some disadvantages. They cannot operate at gains higher than 10^7 due to limitations of the pulse charge capacity per channel [2] and, until recently, a limited lifetime. The lifetime is affected by the large total surface of a microchannel plate which makes it difficult to outgas the channels completely. Internal electron bombardment, therefore, generates ions through electron stimulated desorption. These bombard the cathode backwards with a kinetic energy at the order of keV(s) (depending on MCP bias voltage) and reduce its quantum efficiency [3, 4]. Furthermore, as the cumulative charge handled by the MCP plane increases, the gain decreases. Both effects limit the useful lifetime of MCP-PMTs without proper MCP modifications to an integrated (or cumulative) anode charge (IAC) of about $0.5\,\mathrm{C/cm^2}$.

A novel MCP technology using glass microcapillary array substrates functionalized by the application of resistive and secondary emissive layers using atomic layer deposition (ALD) significantly improved the quality of MCP plates. Photomultipliers with the ALD coating of the MCP plates are characterized by an excellent lifetime reaching $5\ \mathrm{C/cm^2}$ or even higher as reported by the Lehmann group [4].

The time-of-flight (ToF) detectors of the AFP (ATLAS Forward Proton) project [5] use photomultipliers of the miniPlanacon family made by Photonis with two MCP plates, one PMT per ToF detector. They are equipped with a matrix of 4×4 anode pads with a pixel size of $5.8 \times 5.8\,\mathrm{mm^2}$. Each pixel corresponds to one of sixteen L-shaped fused silica bars forming the optical part of the detector. The detection of passing protons (originating from proton-proton collisions at the LHC) is based on Cherenkov light production in the bars. A typical diffractive proton normally passes four bars in one of four rows of the detector. Each row is called a train. Until 2018, a yield of 15-20 photoelectrons (P_e) was achieved per pixel ($60 - 80$ photoelectrons in total per proton in a train) [6]. Since then the yield has increased by a factor of 1.6 [7] due to technological improvements in the production of the bars.

As the anode pads share the same MCP, parasitic crosstalk among the pads affects their output signals. It consists of the electronic crosstalk discussed in the next section and the charge sharing which we briefly describe here. A Cherenkov light pulse emitted in a bar of the ToF detector is almost uniformly distributed across an area of 6×5 mm^2 at the output of the bar on the photomultiplier window [7]. The correspondingly generated charge cloud leaving the MCP pores partly hits anode pads in adjacent pixels at the same time. This effect is known as the charge sharing crosstalk. The charge sharing is less pronounced in tubes with a shorter distance between the anode pads and the MCP output plane [4]. As mentioned above, one proton hits four bars in a train of the ToF resulting in the uniform illumination of one row of four photomultiplier pixels. The charge sharing among pixels in that row is not an issue because it does not cause a loss of timing resolution (the signal arrives at the same time for all four channels due to detector geometry) and any pulses due to the charge sharing towards pixels in adjacent rows can easily be rejected. This form of crosstalk can be controlled primarily by two mechanisms: restricting the channel area that the light can hit and by the reduction of the anode gap by the manufacturer.

Two non-ALD XPM85112 tubes with two MCP plates in each, utilizing $10\,\mu$m pores, were used for Run 2 of the LHC (Large Hadron Collider) at CERN in 2017. The first one had an MCP resistance of $48\,\mathrm{M\Omega}$ and a reduced anode gap of 0.6 mm. The latter one was equipped with MCP plates with a total resistance of $17\,\mathrm{M\Omega}$ and a standard anode gap of 2.9 mm. The ToF detectors were each exposed to the rate of 4 MHz of the signal protons per train (per four pixels) resulting in a total proton flux through each ToF detector of $4.8 \cdot 10^{13}$ during the entire 2017 operation. Both photomultipliers reached an IAC of approximately $2.4\,\mathrm{C/cm^2}$ during this period. This resulted in the degradation of their quantum efficiencies and a drop in the overall performance [8]. Besides this, the PMT gain decline due to high rates of incoming protons negatively affected the performance of the detector [9].

This behaviour was measured in laboratory laser tests and reported in [10]. As stated there, the maximum effective rate estimate (above which the gain declines) is inversely proportional to the MCP resistance, the intrinsic gain (at low kHz rates), and the number of photoelectrons produced by the photocathode. If the last two parameters increase, the amount of the generated charge increases whilst the higher MCP resistance impedes its fast charge draining. Thus, the lower MCP resistance helps achieve better rate capability. The same holds for the lower number of photoelectrons and lower gain, but such PMT rate behaviour improvement is at the expense of the deterioration of its timing resolution [10].

These facts led us to require the following from the MCP-PMTs intended for Run 3 of the LHC (in which the expected proton rate will be 20 MHz per train): an MCP resistance below $30\,\mathrm{M\Omega}$; a proper ALD coating to extend the lifetime of the tube above $10\,\mathrm{C/cm^2}$; and the ability to work at low intrinsic gains at the order of 10^3 so as to shift the maximum light pulse rate above 20 MHz without a significant decline of the operational gain and timing performance due to saturation. Photonis produced the three miniPlanacon XPM85112-S-R2D2 PMTs for us. We modified the backend electronics of the tubes in cooperation with Photonis to suppress the electronic crosstalk among pixels. The next section describes the three photomultipliers and the backend modifications.

2. Tested devices and their modifications

Based on our experience from Run 2 of the LHC we decided to use new MCP-PMTs for Run 3 of the LHC (in which the expected proton rate will be 20 MHz per train). The three miniPlanacon XPM85112-S-R2D2 PMTs produced by Photonis for us are: S/N 9002196 (an MCP resistance of $44\,\mathrm{M\Omega}$), 9002199 ($35\,\mathrm{M\Omega}$), and 9002200 ($27\,\mathrm{M\Omega}$). Later in the paper we often identify them using the last four digits of the S/N only. The spread and deflection of the MCP resistances from the $< 30\,\mathrm{M\Omega}$ requirement are probably due to difficulties in keeping to this parameter during production, particularly with regard to the ALD coating made by Arradiance LLC. They have a fused silica entrance window and a Bialkali photocathode. Their two-stage MCP is ALD-coated (resistive and secondary emissive layers) by Arradiance LLC to achieve an extended lifetime above $10\,\mathrm{C/cm^2}$. We intend to operate them at a low intrinsic gain of $2 \cdot 10^3$ to shift the maximum proton rate (at which timing does not yet deteriorate) above 20 MHz. All these photomultipliers are produced with a matrix of 4×4 pixels defined by square anode pads with a size of $5.8 \times 5.8\,\mathrm{mm^2}$ and a spacing gap of 0.6 mm between them. We decided to modify the back end electronics of the PMTs to fit into the new design of the AFP detector and to suppress negative electronic crosstalk.

Furthermore, one of the PMTs (9002200) featured a reduced anode gap of 0.6 mm (which is much lower than the standard gap of 2.9 mm present in the other two pieces) in an attempt to reduce charge sharing among the anode pads. We will evaluate this later in the paper.

Standard XPM85112 photomultipliers are equipped with two 16-pin arrays of signal output connectors, each consisting of eight signal-ground pairs of pins. In the past, we developed an eight-channel first stage pre-amplifier (called PA-a) designed to directly connect with the block (see Figure 1a). Such a configuration, however, was a concentrated source of heat. For the new Run 3, the compact PA-a modules were replaced with a set of in-line one-channel preamplifiers equipped with MMCX male connectors on the end towards the PMT and a 1.7 m long coaxial cable with the same MMCX ending on the other side (see Figure 1b). This solution allows for better protection against outside electromagnetic interference, easier replacement of any damaged PA-a, and better heat removal through the large overall surface area. For this reason, we needed to modify the layout of the output pins of the new PMTs and add MMCX female connectors to them.

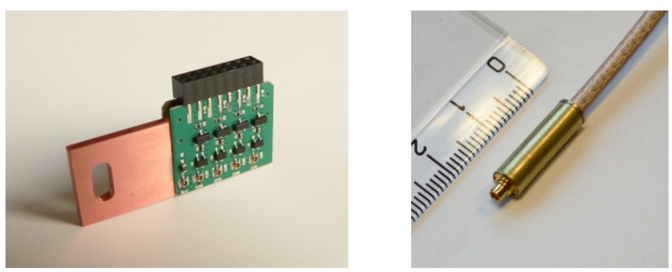

(a) (b)

Figure 1: (a) Eight-channel PA-a module with a copper chiller to be connected to the original design of the PMT and its holder, (b) in-line one-channel version with MMCX connector for the new design of the ToF detector.

The electronic crosstalk among the anode pads is present mostly due to the shared MCP output electrode (MCP-OUT) and existing capacitance between the MCP output plane and the anode pads. This distorts the shape of the signal rising edge and deteriorates the timing performance of the PMT. Figure 2a shows an equivalent circuit of the original photomultiplier design by Photonis. The real electronic components are in a black colour, while the parasitic impedances are indicated in grey. Note the MCP-OUT BIAS part is realized by four parallel branches on the PMT backend (one per each side), whereas only one of them is shown in the scheme. The yellow rectangle represents a nickel strip (50 um thick and 2 mm wide) which connects MCP-OUT BIAS on the backend side with the MCP-OUT electrode plane. The bias resistor R_b and the capacitor C_b form the high-frequency grounding of the MCP-OUT plane together with the intrinsic impedance L_s of the strip. The intrinsic resistance of the strip is negligible with respect to the R_b and it is omitted here. When a developing charge cloud propagates to the MCP-OUT plane, a parasitic crosstalk voltage arises on this grounding part. Its magnitude heavily grows with the value R_b of the bias resistor. The parasitic voltage is shared among all the anodes of the PMT through the capacitances C_{a1}. The bias resistor R_b is a load resistor for the MCP-OUT electrode and it is meant for the readout of the whole MCP output signal. It has no function with regard to a separate readout of individual pixels. Removing the bias resistor is one way of reducing the crosstalk as was done in the ALICE experiment [11]. Moreover, ALICE halved the anode capacitance (C_{a2}) through the optimisation of wire lengths and the ground location. This further led to a decrease in the undesirable crosstalk between adjacent anode pads [11]. Segmentation of the MCP-OUT plane is another way to suppress the electronic crosstalk. This approach was taken in the Hamamatsu photomultiplier SL10 in the frame of the Super-KEKB project [12].

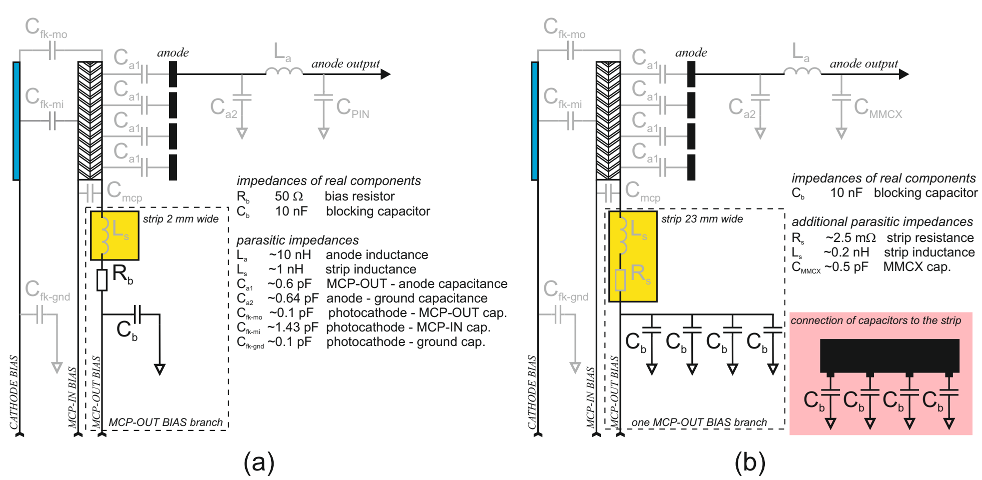

Figure 2: Semi-realistic electronical circuit of (a) the original MCP-PMT XPM85112 by Photonis, (b) the modified design. Real electronic components are in black and parasitic impedances are in grey. The pink inset shows how capacitors are connected to the extended strip.

We were inspired by the approach used in the ALICE experiment and proposed a similar solution without the bias resistor and with various additional modifications aimed to decrease the unwanted capacitances and inductances (see Figure 2b). All these modifications were done in cooperation with Photonis. In Figure 2b, the bias resistors are missing and only a parasitic resistance R_s of the strip is included in each MCP-OUT BIAS branch. The width of the Nickel strips is now 23 mm on three of the four branches. The last one, close to a high-voltage connector, contains a Nickel strip 12 mm wide due to the spatial limitations (see Figure 3a). Besides this, each branch is equipped with four or two (on the branch with the shorter strip) parallel 4.7 nF capacitors C_b distributed equally across the Nickel strip (see the pink inset in Figure 2b). In this design, the high-frequency grounding is formed by these capacitors and the strip impedance (given by R_s and L_s) which is low. Thus, the crosstalk strength is lower with this design.

Like the original design by Photonis, the back end electronics consists of two printed circuit boards (PCBs): the bias PCB and the anode PCB, each with a size of 32×32 mm^2 (see Figures 3a and 3b). The bias PCB has four layers. It contains all the above-mentioned modifications, and it is additionally equipped with an NTC (Negative Temperature Coefficient) thermistor for monitoring the PMT temperature. A black HV input block is bonded to the bias PCB. It includes high-voltage input cables from a high-voltage divider as well as the signal cables of the thermistor. The anode PCB is designed for equal wiring of all the output anode signals and to mount the MMCX female connectors (see Figure 3b). The distribution of the connectors follows the original spatial distribution of the anodes output pins. In the original design, the distance between both PCBs is around 5 mm. The distance is shortened to 2 mm in the modified design. The original ground connections between PCBs of four 1 mm wide Nickel strips on their corners were replaced by 4 mm wide strips as seen in Figure 3c. Figure 3d shows an assembled prototype of a modified XPM85112.

3. Measurement setup

A scheme of the setup can be seen in Figure 4. The measurements were performed using the Hamamatsu M10303-29 laser system. The laser head in use had a wavelength of 405.6 nm and 64.9 ps long pulses. The light from this laser was routed through neutral density filters (OD 0-8) and towards the PMT using two optical fibres with a solarized 200 μm core and an overall

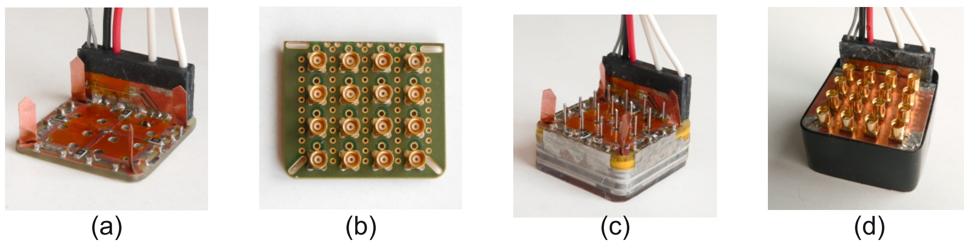

Figure 3: Snapshots from the construction of a prototype of the modified version of the photomultiplier XPM85112: (a) the bias PCB equipped with a black HV input block and four Nickel strips for a grounding connection with the anode PCB, (b) the anode PCB with MMCX female connectors, (c) the prototype after installation of the bias PCB and without the anode PCB, (d) the assembled prototype with both PCBs.

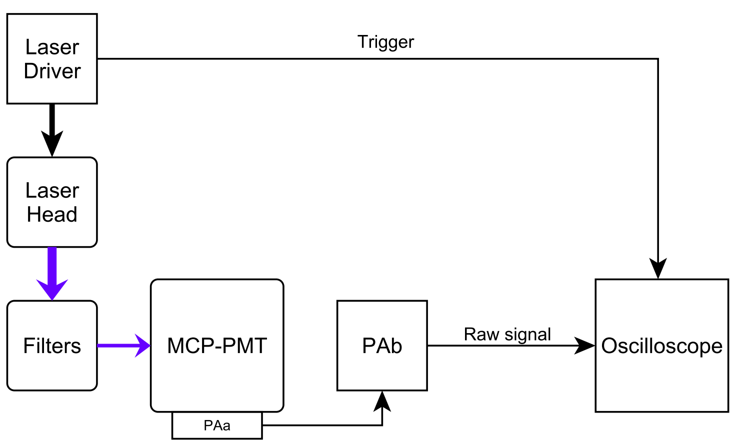

Figure 4: The measurement setup scheme. In some cases, the amplifiers were left out to get a single photoelectron reference charge for the PMT gain measurements.

length of 2 m. The second fibre was either directly attached to the PMT front face through a fixed collimator to illuminate only the centre part of the channel (in the case of gain measurements, where we aim to eliminate any losses to neighbouring channels due to charge sharing) or routed to an adjustable focus collimator to expand the beam in a dark box over a distance of ~ 50 cm to illuminate the PMT in a uniform fashion. A 3D printed custom mask (Figure 5) was used to select the desired channels for illumination, leaving the rest covered. The mask replicated the shape and layout of the fused silica cherenkov bars used in the AFP ToF system (5×6 mm rectangles, centred over the PMT channels). A single channel or an entire column of four channels was used in the measurements, depending on what the goal was. The full column scenario represented the typical response of the AFP ToF system, where a series of four bars is hit by each passing particle.

The PMT body was wrapped with electromagnetic shielding tape and placed in an aluminium dark box to improve its shielding from outside interference. The signal pulse from the PMT was typically amplified using the custom broadband amplifiers with two stages (PAa+PAb) mentioned earlier and read out by an oscilloscope (LeCroy WavePro 806Zi-B with a 6 GHz bandwidth and a 40 GS/s sampling rate), which was triggered by the laser driver sync out signal.

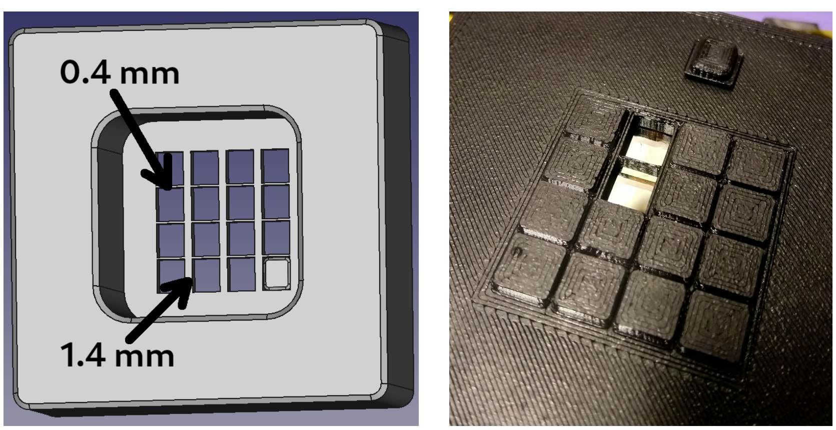

Figure 5: The mask used to select the active channels using individual plugs. The dead space gap sizes at the channel boundaries are marked on the left.

4. Measurement design and results

4.1. Gain curves

Each PMT was subjected to several different measurements. The first one of those was always the gain curve measurement using the pulse charge method. This method is based on integrating the current from the PMT channel being tested when struck by a single photon. For signal to be produced at all, the photon needs to be converted to a photoelectron which in turn has to be accepted and multiplied by an MCP pore, therefore, passing both quantum and collection efficiencies. The charge is obtained by integrating the voltage waveform and dividing it by the known load of $50\,\Omega$. Doing this with no amplifiers and with single photon events at high gain, we can divide the integrated charge by the elementary charge e to get the absolute gain. This is then repeated with amplifiers to get their precise gain. The amplifiers then allow us to measure at a lower PMT gain without losing the signal peak in noise. When the amplified single-photon pulse becomes too weak at around 1750 V, we continue with stronger light pulses of about 5 Pe detected, stitching the measurements together at that point (which is measured at both light levels). This stitching is done a second time at around 1600 V, switching to $\sim 50\,\mathrm{P_e}$ pulses that are observable even at gain as low as 10^3. The resulting gain curves are shown in Figure 6.

The difference in the gain curves measured (blue) as compared to the specification points (yellow) can be attributed to different measurement methods (pulse charge vs current method used by the manufacturer) and the typical slightly changing gain of individual PMT channels. When the gain curve is corrected by a fixed factor to match the 10^5 gain point from the specification, it hits the other specification points with an error of only $1-4\,\%$ (red curve). This tells us the gain measurement was performed correctly and the differences can really be attributed to the measurement method. In particular, our pulse method excludes collection efficiency and takes into account only electrons which are collected and multiplied by the MCP. In contrast, the current method using constant illumination through which the specification was determined includes the collection efficiency in the results. In essence, the ratio between the two curves is a rough measurement of the collection efficiency, which is typically $\sim 50\,\%$ in this type of MCP-PMTs [13].

When the obtained gain curves are later used to determine the number of photoelectrons, only the ratio between the gains at two points on the curve is important and, therefore, the original and corrected curves yield the same results. However, one has to be careful which curve is used when setting up the gain of the PMT itself.

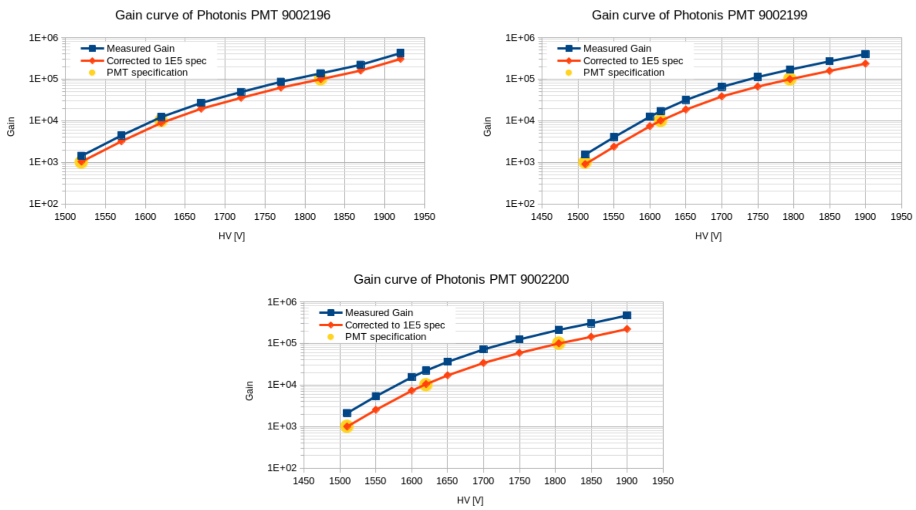

Figure 6: Gain curves of the three PMTs subject to our tests. Yellow points come from the manufacturer's specification. The blue curve is our result with reference to the single-photon charge we measured; the red curve is that curve corrected to match the 10^5 gain point from the PMT specification.

4.2. Timing resolution (TTS)

The timing resolution of the devices being tested was determined by measuring the transit time spread (TTS), the single photoelectron timing resolution. The highest gain data from gain curve measurement, where only single photons were typically detected, were used for this. All of the PMTs tested here have TTS of $38.8 \pm 0.5\,\mathrm{ps}$ (measured as $42 \pm 0.5\,\mathrm{ps}$ before laser pulse width subtraction). An example plot and the fit can be seen in Figure 7.

4.3. Gain behaviour after high rate PMT saturation

As previously reported in [10], the earlier generation of single layer ALD treated long-life MCP-PMTs suffered from extended gain deterioration after being saturated by a high photon flux, which only slowly recovered to the original values. The tubes evaluated here use a double ALD layer (denoted as R2D2) and were subject to the same test which showed a completely different behaviour pattern. As can be seen in Figure 8, the gain actually increases

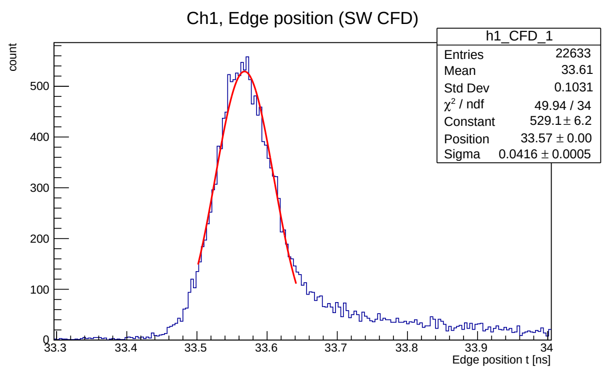

Figure 7: TTS of PMT 2196 at 1920V. The tail on the right of the peak is caused by photoelectrons that bounce from the MCP front face and are accepted by a pore later [14]. When the histogram range is extended to cover the whole tail (spanning $\sim 2.5\,\mathrm{ns}$), the RMS rises to $0.29\,\mathrm{ns}$.

by up to $20\,\%$ when returning to low rates ($10\,\mathrm{Hz}$) after a saturated state ($20\,\mathrm{MHz}$ of $25\,\mathrm{P_e}$ pulses for 1 minute).

The recovery does not reach the original value within the 30-minute test and seems instead to stabilize at $110\,\%$ according to the fit parameters. However, when the PMT is not powered, the recovery is accelerated compared to this measurement and gain reaches the original value under half an hour (deviation of less than $1\,\%$ from the pre-saturation level). This information was utilized when preparing the measurement protocol for the rate capability tests (inserting waiting periods of 30 minutes) in order to prevent the influence of previous high-rate measurements on the baseline gain.

4.4. Rate capability

The rate capability of the PMT is of the utmost importance in our ToF system. The rates of incoming protons passing the detector may reach $20\,\mathrm{MHz}$ in Run 3 of the LHC as the luminosity at interaction points is increased. Thus, we need to show that the PMTs can operate under these conditions without losing too much gain (manifesting as a lower efficiency of our ToF system) or timing resolution. To aid the rate capability, we use a low PMT gain of 2000 (with respect to the red, current method gain curves in Figure 6, corresponding to ~ 4000 pulse gain, which excludes collection efficiency). With the expected number of photoelectrons of $20 - 30$ per proton in each channel hit and a $20\,\mathrm{MHz}$ detection rate, the required rate capability is $\sim 1\,\mu\mathrm{A/cm}^2$ in terms of anode current density.

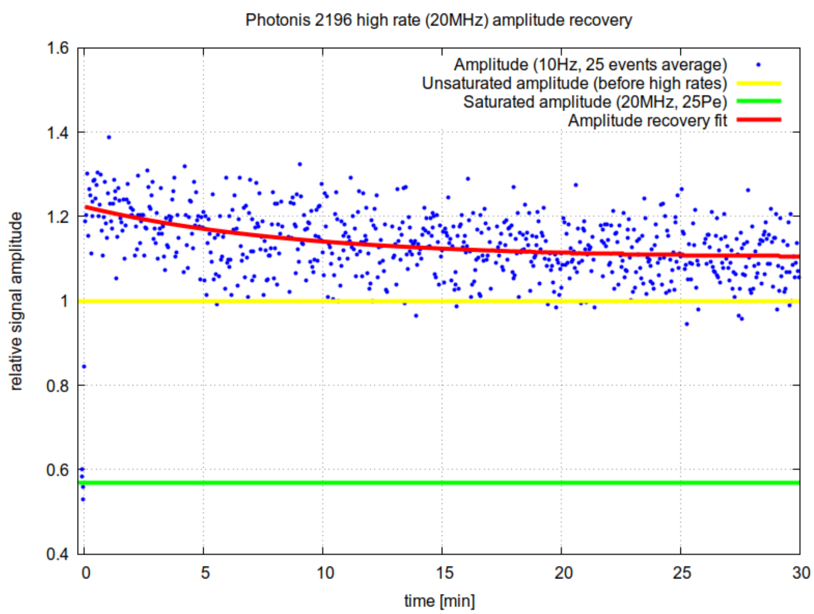

Figure 8: Gain behaviour of PMT 2196 when recovering from saturation, seen as changes in mean amplitude. The $25\,\mathrm{P_e}$ pulse rates were reduced from $20\,\mathrm{MHz}$ ($\sim 1\,\mu\mathrm{A/cm^2}$) to $10\,\mathrm{Hz}$ at $t = 0$. Each blue dot represents the average amplitude of 25 pulses for better plot clarity. The point near $t = 0$ at ~ 0.85 contains partially high and low rate data and is, therefore, an artefact of the switch to low rates.

As four channels in a row are hit in a typical detection event, we set up our channel mask accordingly to open a single row of channels across the PMT. This has the most impact on the timing measurement by allowing for the averaging of the four channels, but it has only a marginal impact on the rate limit [10], as the charge per area is the same as if a single channel had been opened only.

The number of photoelectrons (P_es) in the measured channels was determined as the ratio of the median area under waveform as compared to a single P_e measurement, using the gain curve to correct for the PMT gain difference (single P_e measurements require high gain $\geq 10^5$). We aimed to obtain data at P_e of 25 and 50, with some small variations across the PMTs due to setup (filter) limitations.

The rate scans were performed from 10 kHz up, with this lowest rate point serving as a reference for the relative gain determination. The gain ratio was calculated using the median area under waveform values. If, however, a simple amplitude was used instead, the results would have been essentially identical.

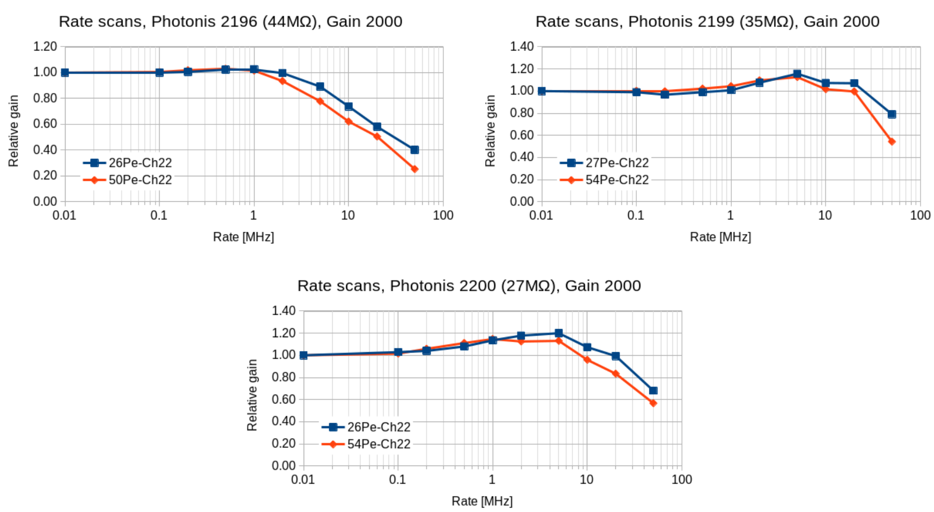

Figure 9: Relative gain during rate scans. Relative gain values at 20 MHz are in Table 1. 20 MHz rate of $\sim 25\,\mathrm{P_e}$ pulses corresponds to anode current of $\sim 1\,\mu\mathrm{A/cm^2}$.

Figure 9 shows the relative gain dependence on the pulse rate, where the gain starts to deteriorate at several MHz, varying across the PMT pieces and the number of $P_\mathrm{e}s$ in the pulse. We can easily see that at comparable P_e, the

MCP resistance has a significant influence on the rate limit, with the lower values allowing for higher rates without the gain suffering. A comparison of the gain behaviour and the timing resolution can be found in Table 1.

The timing resolution results originate from the same measurement set and, therefore, the same considerations about P_es apply. The arrival time of the pulse is determined through a software CFD (constant fraction discriminator), thus removing time walk by triggering at 42 % of the pulse height, which was previously determined to yield the best results. A minimum amplitude cut of 12 mV was used as a cut-off threshold for the events, resulting in > 99 % efficiency at sufficient light levels of $\sim 20 P_e$ or more.

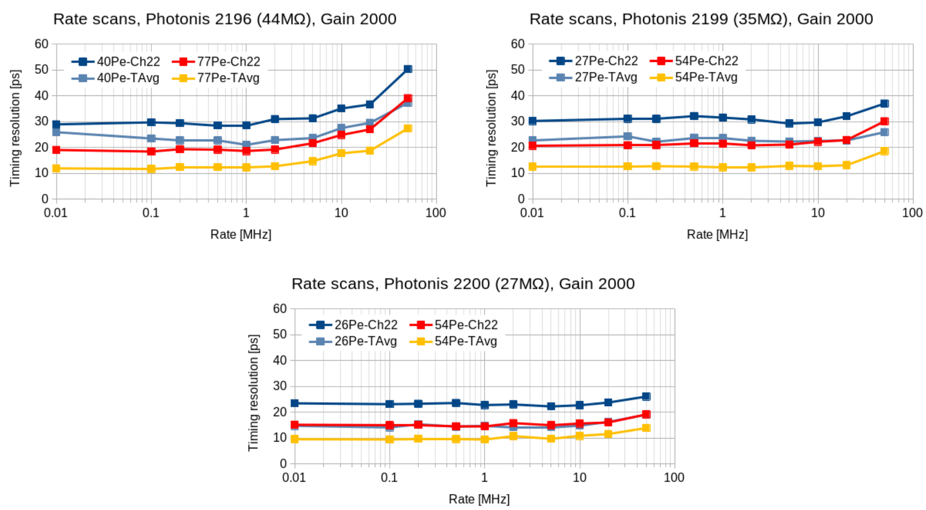

Figure 10: Timing resolution of the detector during rate scans. The TAvg timing is determined as a train (4 channels in a row) average, relevant to our use case. Actual values at 10 kHz and 20 MHz are in Table 1. 20 MHz rate of $\sim 25\,\mathrm{P_e}$ pulses corresponds to anode current of $\sim 1\,\mu\mathrm{A/cm^2}$.

The timing resolution strongly depends on the number of P_es, as can be seen in Figure 10. The train combination (average of arrival times of the four channels forming a train) improves the timing significantly, as expected. In all cases, the timing starts to deteriorate at roughly the same rates as the gain, which can be seen by comparing Figures 9 and 10.

4.5. Crosstalk

As we mentioned in the Introduction, we have studied electronic crosstalk and the crosstalk by charge sharing as separate effects. Whilst the electronic

PMT	MCP R	σ_t (10 kHz)	σ_t (20 MHz)	Gain ratio (20 MHz/10 kHz)
2196	44 MΩ	22.5 ps	39.5 ps	0.58
2199	35 MΩ	22.8 ps	22.8 ps	1.07
2200	27 MΩ	14.8 ps	16.3 ps	0.99

Table 1: Train (4 channel average) timing resolution and relative gain of each PMT when subjected to 10 kHz and 20 MHz pulses of $\sim 25\,\mathrm{P_e}$ ($\sim 0.5\,\mathrm{nA/cm^2}$ and $\sim 1\,\mu\mathrm{A/cm^2}$).

crosstalk from a channel affects all the others approximately to the same extent, the charge sharing takes place only in the immediate vicinity. As the footprint of the ToF bars on the PMT and, therefore, also of the mask openings are asymmetric, we expect to see less charge sharing in the direction where there is a larger width covered/not illuminated (dead area) at the channel boundaries (1.4 mm) as compared to the smaller width (0.4 mm). The smaller anode gap is then expected to give the electrons leaving the MCP less room to spread, reducing the charge sharing in all directions.

The crosstalk measurements were again performed using the channel mask, but with only a single channel open. Four channels were still monitored with the oscilloscope: the open channel, one of its direct neighbours in either direction (where charge sharing and electronic crosstalk mix) and one channel far away (influenced only by electronic crosstalk). A schematic illustration of the channel layout can be seen in Figure 11.

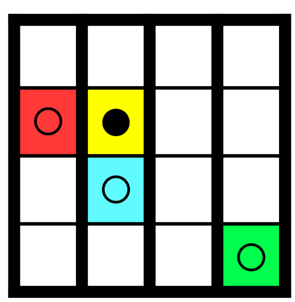

Figure 11: The layout of observed channels during crosstalk measurements. All the channels that are observed are marked with a circle. The sole channel which is illuminated as well as monitored is marked with a filled circle. The colours correspond to the colour coding in Figure 12.

The results match the expectations, as can be seen in Figure 12 and Table 2. Both the reduced anode gap and a wider channel boundary dead area contribute to reducing the crosstalk. In our specific case, the narrow gaps between the ToF bars are along the train, which means the channels are hit together by a single event. As the ToF optical part is designed in such a way that the light from these channels reaches the PMT at the same time, any charge sharing does not present an issue. In the direction across trains, the dead area is wider, limiting the possible charge sharing magnitude and thus producing fewer fake triggers in trains that are neighbours to the one really hit with a proton.

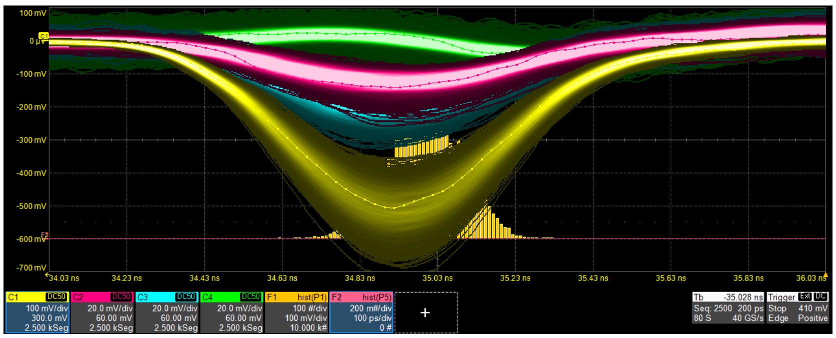

Figure 12: An example of waveforms during the crosstalk measurement of PMT 2199. The yellow waveform (C1) is the illuminated channel; red (C2) is the neighbour across trains; and blue (C3) the neighbour in the same train (charge sharing is the dominant source of crosstalk in C2 and C3). Green (C4) is a channel far away from the one with light, exhibiting the electronic crosstalk only. The colouring scheme follows Figure 11. Note the different vertical scale on C1 (illuminated channel), shrunk by a factor of 5 compared to the crosstalk channels.

Channel spacing	Standard anode gap	Reduced anode gap
In train (0.4 mm)	7.5 %	5.5 %
Next train (1.4 mm)	5.0 %	3.0 %

Table 2: Charge sharing strength as compared to the primary channel signal.

The green (C4) waveform in Figure 12 is the aforementioned electronic crosstalk which manifests as a weak pulse with reversed polarity. This is caused by the inherently imperfect grounding of the shared ground, which is then briefly influenced by the fast signal. Such crosstalk is present in all channels at a similar magnitude of 1.5 % of the signal pulse, but is inseparable from the signal where some crosstalk is present, while influencing its edge and amplitude. For this reason, the proportion of charge sharing is in reality slightly higher than in Table 2, but with respect to the threshold tuning and real detector operation, the values in the table are more relevant than the ones with such correction in place would be.

5. Discussion

Gain curves were determined using the pulse charge method and when corrected for a small, fixed factor difference due to different methods used, they match the gain points specified by the manufacturer very well (a deviation of $1-4\,\%$). These gain curves were later used to determine the proper HV for target gain and to calculate the average number of photoelectrons in each measurement.

The single photoelectron timing resolution (TTS) was determined to be 38.8 ± 0.5 ps in all three pieces. This is about 10 ps worse than most of the devices we tested so far, which were typically just below 30 ps [10, 14].

When comparing tubes with a similar MCP R, the rate capability of these PMTs slightly exceeds the XPM85212/A1-S performance we reported on in [10] There a $36\,\mathrm{M}\Omega$ tube exhibited a $20\,\%$ gain drop already at $1.38\,\mu\mathrm{A/cm^2}$, whereas the 2199 tested here with an almost equivalent MCP R of $35\,\mathrm{M}\Omega$ MCP exhibits the same gain drop at $2.5\,\mu\mathrm{A/cm^2}$. The rate capability again depends strongly on the resistance of the MCP (ones with lower R are handling higher rates better), as expected. At 20 MHz with ~ 25 photoelectrons ($\sim 1\,\mu\mathrm{A/cm^2}$), the two PMTs with the lower resistance ($27\,\mathrm{M}\Omega$, $35\,\mathrm{M}\Omega$) have only a negligible loss of gain whereas the third one ($44\,\mathrm{M}\Omega$) has a loss of gain that is not detrimental to its overall performance. The timing resolution is noticeably impacted only at rates where the gain is starting to be impacted as well. The PMTs can work well at these high rates, particularly thanks to the low gain operation, which draws less charge per pulse from the MCP.

The PMTs do not exhibit the prolonged gain drop as those evaluated in [10]. On the contrary, after being subject to high rates, the gain is actually temporarily increased. This phenomenon can also explain the gain rise in rate capability plots in Figure 9. The PMT 2196, which is not able to perform at high rates so well, exhibits a different type of behaviour – the gain bump is not explicitly visible in the rate plots, but it contributes instead only to a less steep initial gain decline, since the bump probably occurs at similar rates for all PMTs while keeping the gain equivalent. In order to remove the impact of this gain change effect induced by high rate saturation, all measurements were done with waiting periods of 30 minutes between them.

The crosstalk between the channels was measured as two separate effects. One part is electronic, originating in the capacitive couplings between channels and ground rebound. This has the same impact on all channels within the PMT and is proportional to the primary pulse amplitude ($\sim 1.5\,\%$). The second effect is charge sharing within the PMT, where parts of the generated electron spray hit adjacent anode pads. This strongly depends on the geometry, specifically how close to the channel boundary photons are allowed to land, and also on the anode gap size (a shorter gap means less spreading of the electrons leaving the MCP and less charge sharing).

6. Conclusion

Three pieces of miniPlanacon XPM85112-S-R2D2 MCP-PMTs with modified backend electronics were tested. The tests were performed using a picosecond laser setup, with the focus on timing resolution, while rate capability and crosstalk, gain curves were also determined.

The rate capability of each PMT strongly depends on its MCP resistance, as expected. Low PMT gain operation also allows them to reach a high rate capability, while more focus has to be directed towards proper shielding from interference to maintain a reasonable signal-to-noise ratio. When the PMTs are saturated with too much light, gain starts to drop, and the timing resolution is negatively impacted as well. Recovery from the PMT saturation happens through temporarily increased gain which returns to normal in under half an hour if the PMT is not powered.

Crosstalk between the channels was determined to consist of two types: one with influence over the whole PMT (ground rebound) and the other with influence only on its direct neighbours (charge sharing). The latter is heavily influenced by the anode gap size (a smaller gap allows for less electron spread) and the geometry of the illuminated area of each channel.

7. Funding

The authors gratefully acknowledge the support from the Operational Programme Research Development and Education – European Regional Development Fund, project no. CZ.02.1.01/0.0/0.0/16_019/0000754 of the Ministry of Education, Youth and Sports of the Czech Republic (MSMT); Research Infrastructure for experiments at CERN LM 2018104 (MSMT); Getting new knowledge of the microworld using the CERN infrastructure

LTT17018 (MSMT); Palacky University IGA_PrF_2022_004; and the U.S. Department of Energy DE-SC0011686.

References

[1] A. Lehmann, M. Böhm, A. Britting, W. Eyrich, M. Pfaffinger, F. Uhlig, A. Belias, R. Dzhygadlo, A. Gerhardt, K. Götzen, G. Kalicy, M. Krebs, D. Lehmann, F. Nerling, M. Patsyuk, K. Peters, G. Schepers, L. Schmitt, C. Schwarz, J. Schwiening, M. Traxler, M. Zühlsdorf, M. Düren, E. Etzelmüller, K. Föhl, A. Hayrapetyan, B. Kröck, O. Merle, J. Rieke, M. Schmidt, T. Wasem, E. Cowie, T. Keri, P. Achenbach, M. Cardinali, M. Hoek, W. Lauth, S. Schlimme, C. Sfienti, M. Thiel, Recent developments with microchannel-plate PMTs, Nucl. Instrum. Meth. A 876 (2017) 42–47.

[2] P. Inc., Photomultiplier tubes: Principles and applications, Photonis, Brive, France (2002).

[3] C. Ertley, O. Siegmund, T. Cremer, C. Craven, M. Minot, J. Elam, A. Mane, Performance studies of atomic layer deposited microchannel plate electron multipliers, Nucl. Instrum. Meth. A 912 (2018) 75–77.

[4] A. Lehmann, M. Böhm, W. Eyrich, D. Miehling, M. Pfaffinger, S. Stelter, F. Uhlig, A. Ali, A. Belias, R. Dzhygadlo, A. Gerhardt, K. Götzen, G. Kalicy, M. Krebs, D. Lehmann, F. Nerling, M. Patsyuk, K. Peters, G. Schepers, L. Schmitt, C. Schwarz, J. Schwiening, M. Traxler, M. Düren, E. Etzelmüller, K. Föhl, A. Hayrapetyan, K. Kreutzfeld, O. Merle, J. Rieke, M. Schmidt, T. Wasem, P. Achenbach, M. Cardinali, M. Hoek, W. Lauth, S. Schlimme, C. Sfienti, M. Thiel, Lifetime of MCP-PMTs and other performance features, J. Instrum. 13 (2018) C02010.

[5] J. Lange, L. Adamczyk, G. Avoni, E. Banas, A. Brandt, M. Bruschi, P. Buglewicz, E. Cavallaro, D. Caforio, G. Chiodini, L. Chytka, K. Ciesla, P. Davis, M. Dyndal, S. Grinstein, K. Janas, K. Jirakova, M. Kocian, K. Korcyl, I. Paz, D. Northacker, L. Nozka, M. Rijssenbeek, L. Seabra, R. Staszewski, P. Swierska, T. Sykora, Beam Tests of an Integrated Prototype of the ATLAS Forward Proton Detector, J. Instrum. 11 (2016) P09005.

[6] L. Nozka, A. Brandt, M. Rijssenbeek, T. Sykora, T. Hoffman, J. Griffiths, J. Steffens, P. Hamal, L. Chytka, M. Hrabovsky, Design of Cherenkov bars for the optical part of the time-of-flight detector in Geant4, Opt. Express 22 (2014) 28984–28996.

[7] L. Nozka, A. Brandt, K. Cerny, M. Hrabovsky, T. Komarek, F. Krizek, D. Mandat, M. Milovanovic, M. Rijssenbeek, P. Schovanek, T. Sykora, V. Urbasek, J. Zatloukal, Performance studies of new optics for the time-of-flight detector of the AFP project, Opt. Express 28 (2020) 19783–19796.

[8] Cerny, K. on behalf of the ATLAS Collaboration, Performance study of the ATLAS Forward Proton Time-of-Flight Detector System, in: The 28th International Workshop on Vertex Detectors 2020, 2020, p. 055.

[9] Sykora T. on behalf of the ATLAS Collaboration, ATLAS Forward Proton Time-of-Flight Detector: LHC Run2 performance and experiences, J. Instrum. 15 (2020) C10004.

[10] T. Komarek, V. Urbasek, A. Brandt, V. A. Chirayath, V. Chytka, M. Hrabovsky, L. Nozka, M. Rijssenbeek, T. Sykora, Timing resolution and rate capability of Photonis miniPlanacon XPM85212/A1-S MCP-PMT, Nucl. Instrum. Meth. A 985 (2021) 164705.

[11] Melikyan, Yu. A. on behalf of ALICE Collaboration, Performance of Planacon MCP-PMT photosensors under extreme working conditions, Nucl. Instrum. Meth. A 952 (2020) 161689.

[12] K. Inami, T. Mori, T. Matsumura, S. Kurimoto, K.and Hasegawa, Y. Suzuki, T. Murase, Y. Yurikusa, M. Akatsu, Y. Enari, T. Hokuue, A. Tomita, N. Kishimoto, T. Ohshima, T. Ihara, H. Nishizawa, Cross-talk suppressed multi-anode MCP-PMT, Nucl. Instrum. Meth. A 592 (2020) 247–253.

[13] D. Orlov, T. Ruardij, S. D. Pinto, R. Glazenborg, E. Kernen, High collection efficiency MCPs for photon counting detectors, Journal of Instrumentation 13 (01) (2018) C01047–C01047. doi:10.1088/1748-0221/13/01/c01047.
URL `https://doi.org/10.1088/1748-0221/13/01/c01047`

[14] A. G. Brandt, Development of a 10 picosecond time-of-flight Counter, Tech. rep., Univ. of Texas, Arlington, TX (United States) (3 2010). doi:10.2172/973786.
URL https://www.osti.gov/biblio/973786